12 Jun 2023

Magnetic-Induced Swing Adsorption Over Iron Oxide/13X: Effects Of Particle Size And Oxide Phase On Sorbent Regeneration In Ethylene/Ethane Separation

Khaled Baamran

Ali A. Rownaghi
Missouri University of Science and Technology, rownaghia@mst.edu

Fateme Rezaei
Missouri University of Science and Technology, rezaeif@mst.edu

Recommended Citation

K. Baamran et al., "Magnetic-Induced Swing Adsorption Over Iron Oxide/13X: Effects Of Particle Size And Oxide Phase On Sorbent Regeneration In Ethylene/Ethane Separation," *ACS Sustainable Chemistry and Engineering*, vol. 11, no. 23, pp. 8603 - 8614, American Chemical Society, Jun 2023.
The definitive version is available at https://doi.org/10.1021/acssuschemeng.3c01468

ACS Sustainable Chemistry & Engineering

pubs.acs.org/journal/ascecg

Research Article

Magnetic-Induced Swing Adsorption over Iron Oxide/13X: Effects of Particle Size and Oxide Phase on Sorbent Regeneration in Ethylene/Ethane Separation

Khaled Baamran, Ali A. Rownaghi, and Fateme Rezaei*

Cite This: *ACS Sustainable Chem. Eng.* 2023, 11, 8603–8614

Read Online

ACCESS | Metrics & More | Article Recommendations | Supporting Information

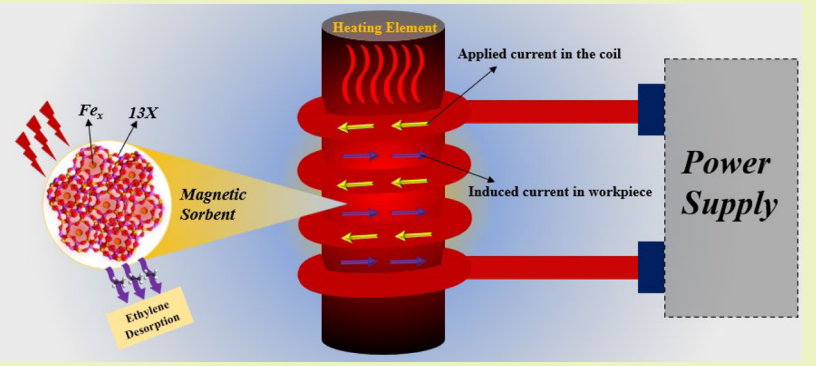

ABSTRACT: Magnetic induction has emerged as a viable method for regeneration of sorbents during separation processes. In this work, we investigated the efficacy of magnetic sorbents comprising iron oxide and zeolite 13X in ethylene/ethane separation *via* a magnetic induction process. The electromagnetic properties of the sorbents were tuned by varying the iron oxide (Fe_2O_3) particle size (30 nm, 100 nm, 5 μm) and iron oxide phase structure (FeO, Fe_2O_3, Fe_3O_4) at 20 wt % loading. The effects of these parameters on adsorption capacity, selectivity, and desorption rates were systematically investigated. The microporosity and surface area of magnetic sorbents were reduced by increasing the particle size of Fe_2O_3 from 30 nm to 5 μm. The results indicated that regardless of iron oxide particle size or phase structure, the C_2H_4/C_2H_6 selectivity ranges between 2.44 and 2.65 for all the magnetic sorbents. The specific heat absorption rate (*SAR*) was increased by ~60% upon increasing the magnetic field intensity from 21.4 to 31.4 mT when the particle size increased from 30 nm to 5 μm. Fe_3O_4 was found to outperform the other phases by exhibiting 91.3 and 93.3% higher *SAR* than Fe_2O_3 and FeO at 31.4 mT, respectively, owing to its unique lattice structure with dual ion states (Fe^{2+} and Fe^{3+}). Fe_3O_4/13X exhibited an ethylene desorption rate of 0.41 mmol/g·min at 21.4 mT, which was 58.5% faster than that under conventional thermal heating. Additionally, the sorbent was found to be highly durable, maintaining its adsorption and desorption capabilities over five consecutive cycles in the magnetic induction swing adsorption (MISA) process, conducted at 25 °C and 1 bar during adsorption and at 31.4 mT during desorption. These results indicate the potential of Fe_3O_4/13X as an effective magnetic sorbent in the MISA process. This study builds on our previous proof-of-concept work on the potential of magnetic sorbents as stimuli-responsive materials for light olefin/paraffin separation.

KEYWORDS: *magnetic sorbent, 13X, Fe_3O_4, induction heating, C_2H_4/C_2H_6 separation*

1. INTRODUCTION

The global chemical industry produces over 170 million tons of ethylene (C_2H_4) each year, typically by thermal decomposition or steam reforming of ethane (C_2H_6).[1−5] To purify the produced C_2H_4, downstream cryogenic distillation is required to remove small amounts of co-existing C_2H_6.[6−9] Considering how energy-intensive this separation process is, significant efforts have been made to replace it with non-thermal methods, such as membrane separation or adsorption.[10−13] In particular, C_2H_4/C_2H_6 separation via adsorption over nanoporous materials has been touted as a promising technology to improve energy efficiency of this process.[14,15] However, adsorptive separation of light olefins/paraffins still remains in its infancy despite significant advances that have been made in sorbents design and discovery over the past few decades.

Received: March 13, 2023
Revised: May 11, 2023
Published: May 26, 2023

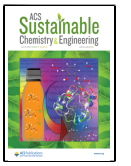

To address high energy requirements of conventional pressure/temperature swing adsorption systems (P/TSA), alternative approaches have been recently proposed, such as magnetic induction swing adsorption (MISA), microwave swing adsorption (MSA), and electrical swing adsorption (ESA), which rely on induction heating, microwave heating, and Joule heating, respectively, to convert electricity to heat.[16−20] In the latter approach, desorption occurs through the sorbent's ohmic resistance which converts electricity to heat. For efficient heating and regeneration, the electric current must be evenly distributed over the sorbent bed, which necessitates uniform connectivity across the bed. Poor electric conductivity can cause hot spots in case of maldistribution, making ESA unsafe. As a result, expanding the ESA process becomes extremely difficult.[21,22] In contrast to ESA, the sorbent in MSA or MISA does not require connectivity or uniform distribution across the bed, rather, it can be heated remotely *via* microwave or magnetic induction. Induction heating technology has recently piqued the interest of researchers, who believe it will soon find its way into the large-scale separation processes.

In induction heating, heat is generated uniformly throughout the material due to localized nanoheaters, and thus is preferred for regeneration of sorbents with low thermal conductivity. Through the application of high-frequency currents, the magnetic field is changed, causing the eddy currents to stabilize and other conductive materials to align domains to alternate their directions, resulting in a rise in temperature and thereby regeneration of the sorbent.[21,23] Despite promises, this technology faces a formidable challenge of poor electromagnetic conductivity of the sorbents, which renders them unresponsive to an external magnetic field. By hybridizing sorbent crystals with magnetic particles, it is however possible to improve the local thermal heating of the sorbent particles *via* alternating magnetic fields. For example, the induction heating of MOF crystals combined with ferrimagnetic $MgFe_2O_4$ has been demonstrated by Sadiq *et al.*[24] in CO_2 desorption. UiO-66@$MgFe_2O_4$ sorbent with a thermal efficiency of 60% was reported to release 100% CO_2 after 240 s of regeneration time at 42 mT, whereas in Mg-MOF-74@$MgFe_2O_4$, a release efficiency of ∼67.3% within 21 min was observed at 55.9 mT.[24,25] Most recently, we investigated the regeneration of magnetic sorbents comprising 13X/Fe_2O_3 and showed that the large particle size of Fe_2O_3 significantly increases the desorption rate due to the high energy absorption at particle size of 5 μm.[26] In a study involving similar magnetic sorbents but using a different phase of iron oxide, such as Fe_3O_4, Gholami *et al.*[21] found rapid thermal regeneration of 13X/20% Fe_3O_4 when exposed to an electromagnetic field. The 13X/20% Fe_3O_4 composite absorbed much higher net energy compared to its counterpart composite 13X/20% Fe_2O_3 with the same particle size (5 μm), owing to the unique lattice structure of Fe_3O_4 with dual ionization states (Fe^{2+} and Fe^{3+}), thereby making it an excellent magnetic absorber.[27,28]

In this work, we aimed at maximizing the desorption rate of magnetic sorbents used in ethylene/ethane separation by increasing the magnetic responsiveness of the materials. For this purpose, six different magnetic sorbents (Fe_{20}/13X) comprising different iron oxide particle sizes (*e.g.*, 30 nm, 100 nm, 5 μm) and different iron oxide phases (*e.g.*, FeO, Fe_2O_3, Fe_3O_4) were developed at fixed 20 wt % iron oxide loading. The unary adsorption isotherms of ethane and ethylene were measured to estimate the adsorption capacity of the synthesized magnetic sorbents. Dynamic adsorption−desorption experiments were performed using binary C_2H_4/C_2H_6 feed to systematically assess the thermal efficiency upon exposure to different magnetic field strengths (*e.g.*, 21.4, 26.4, and 31.4 mT). The effect of iron oxide particle size and phase structure on desorption rate and thermal efficiency was systematically investigated. Finally, a comparison between conventional and induction heating methods and their effects on sorbent regeneration and cooling rate was carried out.

2. EXPERIMENTAL SECTION

2.1. Materials. The following materials were used for sorbent synthesis without further purification: iron(III) oxide nanoparticle (Fe_2O_3, α, 99.5%, 100 and 30 nm), iron(III) oxide microparticle (Fe_2O_3, α, 99.5%, <5 μm), iron(II,III) oxide microparticle (Fe_3O_4, 99.5%, <5 μm), iron(III) nitrate nonahydrate ($Fe(NO_3)_3(H_2O)_9$), iron(II) oxide (FeO, 99.5%, metal basis), and 13X zeolite. All materials were purchased from Sigma-Aldrich except for the FeO and 13X, which were purchased from Alfa Aesar. The ultra-high purity gases used in this study were all obtained from Airgas.

2.2. Synthesis of Fe_{20}(A−D)/13X Sorbents. The wet impregnation method was used for doping iron oxide precursors into 13X zeolite. Briefly, 20% of iron oxide (Fe_{20}) was dissolved in 50 mL of 13X solution, and the solution was then rolled at 60 rpm for 1 day [Fe_{20} = Fe_2O_3 (30 nm), Fe_2O_3 (100 nm), Fe_2O_3 (5 μm), and Fe_3O_4 (5 μm)]. The obtained slurry was dried at 120 °C for 12 h, and the precipitations were grinded into homogeneous powder using a mortar and pestle before being used in experiments. The prepared samples, namely, Fe_{20}(Fe_2O_3, 30 nm)/13X, Fe_{20}(Fe_2O_3, 100 nm)/13X, Fe_{20}(Fe_2O_3, 5 μm)/13X, and Fe_{20}(Fe_3O_4, 5 μm)/13X, were labeled as: Fe_{20}(A)/13X, Fe_{20}(B)/13X, Fe_{20}(C)/13X, and Fe_{20}(D)/13X, respectively, as shown in Table 1.

Table 1. Prepared Samples' Names and Labels Used in This Investigation

sample	sample label
Fe_{20}(Fe_2O_3, 30 nm)/13X	Fe_{20}(A)/13X
Fe_{20}(Fe_2O_3, 100 nm)/13X	Fe_{20}(B)/13X
Fe_{20}(Fe_2O_3, 5 μm)/13X	Fe_{20}(C)/13X
Fe_{20}(Fe_3O_4, 5 μm)/13X	Fe_{20}(D)/13X
[Fe_{20}(Fe_2O_3, 5 μm)/13X]/20% FeO	Fe_{20}(E)/13X
Fe_{20}(Fe_2O_3)/13X (1.4−77 μm)	Fe_{20}(F)/13X

2.3. Synthesis of Fe_{20}(E−F)/13X Sorbents. Fe_{20}(E)/13X was prepared by the exact synthesis method described in Section 2.2 for Fe_{20}(C)/13X. However, when Fe_{20}(C)/13X was synthesized, 20% of FeO was physically mixed with Fe_{20}(C)/13X to produce Fe_{20}(E)/13X, as noted in Table 1. For the synthesis of Fe_{20}(F)/13X, 20% of $Fe(NO_3)_3(H_2O)_9$ (Fe_{20}) was dissolved in 50 mL of 13X solution and stirred vigorously at 400 rpm for 1 h. The obtained precipitate was then dried at 120 °C for 12 h, grinded into homogeneous powder, and calcined in air at 500 °C for 5 h at a 10 °C/min heating rate. The particle size of Fe_{20}(F)/13X was measured using a Microtrac S3500 particle size analyzer and included in Table 1.

2.4. Characterization of Fe_{20}(A−F)/13X Sorbents. The textural properties of the Fe_{20}(A−F)/13X samples were assessed by N_2 physisorption experiments at 77 K on a Micromeritics (3Flex) gas analyzer instrument. All samples [Fe_{20}(A)/13X, Fe_{20}(B)/13X, Fe_{20}(C)/13X, Fe_{20}(D)/13X, Fe_{20}(E)/13X, and Fe_{20}(F)/13X] before analysis were degassed at 350 °C under vacuum for 5 h on a Micromeritics Smart VacPrep instrument. The Brunauer−Emmett−Teller (BET), Horvath and Kawazoe, and nonlocal density functional theory methods were used to determine surface area, pore size distribution (PSD), and pore volume. The magnetic properties of the Fe_{20}(A−F)/13X sorbents were determined by electron paramagnetic resonance (EPR) Bruker instrument. All the samples were exposed to

https://doi.org/10.1021/acssuschemeng.3c01468
ACS Sustainable Chem. Eng. 2023, 11, 8603−8614

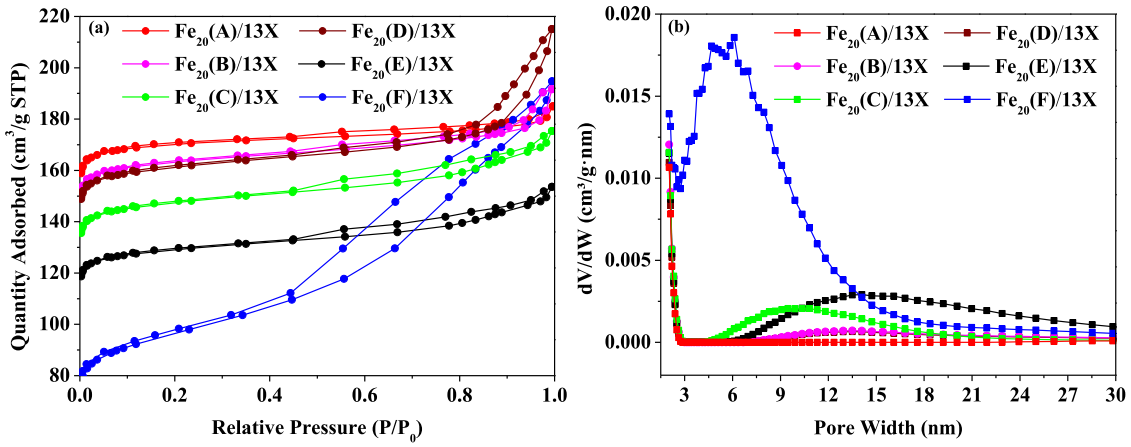

Figure 1. (a) N_2 physisorption isotherms and (b) PSD of Fe_{20}(A−F)/13X sorbents.

a magnetic field in the range of 50−550 mT and the EPR intensity was recorded.

2.5. Adsorption Isotherm Measurements. A volumetric gas analyzer (Micromeritics, 3Flex) was used to measure the unary adsorption isotherms of C_2H_6 and C_2H_4 over the pressure range 0−1 bar. Prior to the measurements, Fe_{20}(A)/13X, Fe_{20}(B)/13X, Fe_{20}(C)/13X, Fe_{20}(D)/13X, Fe_{20}(E)/13X, and Fe_{20}(F)/13X were degassed on a Micromeritics Smart VacPrep instrument under vacuum at 350 °C for 5 h to remove any preadsorbed gases or moisture.

2.6. Magnetic Induction Breakthrough Experiments. An in-house lab setup was used for conducting the dynamic adsorption−desorption experiments under magnetic induction heating, as reported in our prior works.[26,29] For this purpose, a quartz tube with a length of 25 cm and an inner diameter of 1 cm was used for the adsorption−desorption experiments. Nonconductive plastic materials were chosen for the fittings and connectors of the inlet and outlet openings of the column. This was done to avoid heating loss, as metallic materials tend to heat up under induction heating. The magnetic field exposed to sorbents was sourced from an induction heating system (EASYHEAT 1.2 to 2.4 kW-AMBRELL) equipped with an induction coil 4 cm in length, 8 turns, and 2.5 cm in diameter. For each experiment, the temperature profile was recorded using a temperature controller (FOTEMP4-PLUS-P0-V-B) along with a fiber-optic (FO) temperature sensor (OPTOCON, TS3-10MM-02) to ensure accurate temperature measurements. 3.0 g of sorbent mass, 25 °C, and 1 bar were the typical operating conditions used in all breakthrough experiments. The adsorption bed was trapped between two glass wools, and the rest of the column was filled by glass beads. The sorbent was *in situ* activated at 200 °C for 8 h under 20 mL/min of Ar flow rate. Next, the column was cooled down to 25 °C, and simultaneously 5 mL/min flow rate of Ar and 54 mL/min of C_2H_4/C_2H_6 with a feed composition of 50/50 mol % were fed into the bed. The gas flow rates were measured by mass flow controllers, and the outlet gas flow was analyzed by a mass spectrometer (MKS, Cirrus 2). When the bed was saturated with C_2H_6 and C_2H_4, the flow rate of C_2H_4/C_2H_6 was terminated, and the inlet feed of Ar was switched to 20 mL/min, while the magnetic field was turned on at different field strengths (21.4, 26.4, and 31.4 mT). The desorption step was continued until the sorbent bed was fully regenerated from C_2H_6 and C_2H_4. In the cyclic adsorption−desorption experiments, the adsorption step was stopped upon reaching $t_{ads,5\%}$ of the selective adsorbate (C_2H_4) to simulate industrial applications. Subsequently, the flow rate of C_2H_4/C_2H_6 was stopped, the inlet Ar feed was switched to 20 mL/min, and the magnetic field was then turned on with a strength of 31.4 mT. The desorption step was carried out until complete regeneration of the sorbent bed from C_2H_6 and C_2H_4 was achieved, and subsequently the bed was cooled down to 25 °C before the initiation of the next cycle.

2.7. Specific Heat Absorption Rate Measurements. The specific heat absorption rate (*SAR*, W/g) was measured following a procedure reported in our previous work.[24,29] Briefly, the various iron oxides {Fe_2O_3(30 nm), Fe_2O_3(10 nm), Fe_2O_3(5 μm), Fe_2O_3[(5 μm)/20% FeO], Fe_3O_4(5 μm), and Fe_2O_3} were dispersed separately in water first and then each sample was exposed to three different magnetic fields, followed by recording the temperature gradients, as shown in Figure S1. The estimated *SAR* values are summarized in Tables S1−S3. For specific heat capacity (C_p) measurements, a differential scanning calorimetry (DSC, 2010 V4.4E instrument) was used to measure the heat capacity of the magnetic sorbents.

3. RESULTS AND DISCUSSION

3.1. Characterization of Fe_{20}(A−F)/13X Sorbents. The N_2 physisorption isotherms and PSD profiles of Fe_{20}(A−F)/13X sorbents are depicted in Figure 1, and the corresponding textural properties are summarized in Table 2. The Fe_{20}(A−F)/13X sorbents displayed type I−IV isotherms, indicative of their microporous−mesoporous structure.[30,31] The PSD profiles in Figure 1b confirmed the existence of both micro- and mesopores in the range of 2−30 nm for these sorbents. However, the BET surface area and pore volume varied across Fe_{20}(A−D)/13X sorbents due to the different iron oxide particle sizes (30 nm, 100 nm, 5 μm) and iron oxide phases (Fe_2O_3, Fe_3O_4). First looking at Fe_{20}(A−C)/13X, it can be noted that the small particle size of Fe_2O_3 [*e.g.*, Fe_{20}(A)/13X] retained the microporosity of 13X, whereas the surface area and pore volume reduced with increasing the particle size, as in Fe_{20}(B)/13X and Fe_{20}(C)/13X sorbents, indicating that doping Fe_2O_3 nanoparticles does not significantly alter the microporous character of 13X. Comparing the same particle size (5 μm), as in Fe_{20}(C)/13X with different iron oxide phases (*e.g.*, Fe_3O_4) as in Fe_{20}(D)/13X, the surface area and micropore pore volume were increased, implying that Fe_3O_4 enhanced the microporosity of 13X compared to Fe_2O_3. The

Table 2. Textural Properties of Fe_{20}(A−F)/13X Sorbents

sorbent	S_{BET} (m^2/g)	V_{micro} (cm^3/g)	V_{meso} (cm^3/g)	d_p (nm)
Fe_{20}(A)/13X	670	0.246	0.039	2.1, 2.2, 2.3, 2.4
Fe_{20}(B)/13X	641	0.231	0.065	2.1, 2.2, 2.4, 2.5
Fe_{20}(C)/13X	578	0.206	0.065	2.2, 6.1, 8.4, 10.5
Fe_{20}(D)/13X	632	0.226	0.106	2.1, 2.2, 2.3, 2.4
Fe_{20}(E)/13X	555	0.171	0.051	2.2, 8.1, 9.4, 12.5
Fe_{20}(F)/13X	362	0.097	0.204	3, 5, 6, 7.2, 9

https://doi.org/10.1021/acssuschemeng.3c01468
ACS Sustainable Chem. Eng. 2023, 11, 8603−8614

Fe_{20}(C)/13X was further physically mixed with 20% FeO, as in Fe_{20}(E)/13X because FeO was used as the metal base, and the results showed that the surface area and pore volume of Fe_{20}(C)/13X were slightly reduced due to the reduction of adsorption mass per volume compared to Fe_{20}(C)/13X.[3] Finally, Fe_{20}(F)/13X exhibited the lowest surface area compared to other samples, primarily due to its lowest microporosity.[31] The different textural properties of Fe_{20}(A−E)/13X and Fe_{20}(F)/13X could be ascribed to the different synthesis methods and iron precursors used, which caused Fe_{20}(F)/13X to exhibit a particle size distribution of 1.4−77 μm. Xia *et al.*[32] investigated the textural properties of hierarchical porous carbons and found that the carbon with the lower surface area had a larger mesopore volume.

From Table 2, the BET surface area and micropore volume of Fe_{20}(A)/13X were measured to be 670 m^2/g and 0.246 cm^3/g, respectively, whereas for Fe_{20}(B)/13X and Fe_{20}(C)/13X, these values were reduced by ∼13% (*e.g.*, 641 and 578 m^2/g) and 16% (*e.g.*, 0.231 and 0.206 cm^3/g), respectively, albeit with 40% mesoporosity enhancement. This trend of decline in BET surface area and micropore volume was also observed in Fe_{20}(E)/13X due to physical mixing with larger particles of FeO that reduced the sorbent mass per volume. However, when a different iron oxide was used, such as Fe_{20}(D)/13X, these values were increased by 8.5% (*e.g.*, 632 m^2/g) and 8.8% (*e.g.*, 0.226 cm^3/g), respectively, compared to Fe_{20}(C)/13X. The mesopore volume was also enhanced from 0.065 to 0.106 cm^3/g for these materials. In conclusion, these results highlight that the larger particle sizes of iron oxide, the lower BET surface area and micropore volume—which could likely be attributed to the blockage of pores—and that Fe_3O_4 iron oxide can maintain sorbent's microporosity better than Fe_2O_3.

The sorbent's magnetism ability with varied iron oxide particle size was characterized by the EPR analysis to determine the degree of responsiveness of the magnetic sorbents, and the results are depicted in Figure 2. As can be seen, increasing the Fe_2O_3 particle size from 30 and 100 nm [Fe_{20}(A)/13X and Fe_{20}(B)/13X] to 5 μm gave rise to enhanced EPR spectrum absorbance, as in Fe_{20}(C)/13X. However, when Fe_2O_3 was replaced by Fe_3O_4 with the same particle size, Fe_{20}(D)/13X absorbed the highest amount of heat upon exposure to the magnetic field. Adding 20% FeO to Fe_{20}(C)/13X as in Fe_{20}(E)/13X enhanced its EPR intensity, which was between that of Fe_{20}(C)/13X and Fe_{20}(D)/13X. On the basis of these results, it can be deduced that there is a strong relation between the heat absorption rate and particle size/phase of iron oxide in the magnetic sorbents. The increase in heating with particle size stems from enhanced anisotropic energy property of ferromagnetic materials, which results in higher electronic vibrations that heats the magnetic material.[26,33] On the other hand, the absorption rate enhancement in Fe_3O_4 is attributed to the dual ionization state (Fe^{2+} and Fe^{3+} ions), which makes Fe_3O_4 easily attracted to an external magnetic field compared to Fe_2O_3, which only contains Fe^{3+} ions, thereby resulting in higher electromagnetic waves.[27]

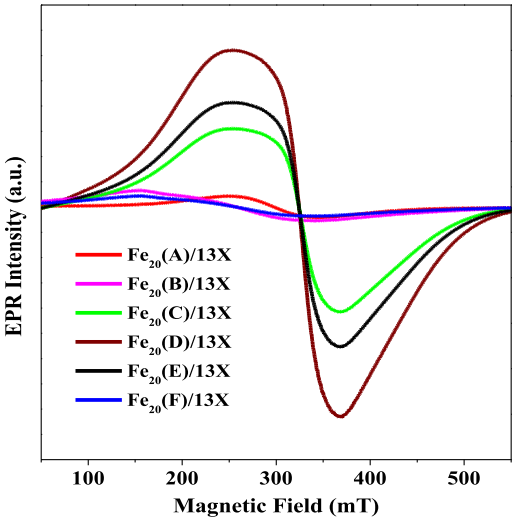

Figure 2. EPR spectra of Fe_{20}(A−F)/13X sorbents.

The corresponding *SAR* values were calculated for all sorbents following a method reported in the literature,[24] and the results are summarized in Table 3. The temperature gradient profiles from the *SAR* experiments are also shown in Figure S1. As expected, increasing the magnetic field from 21.4 to 31.4 mT resulted in a 40% increase in specific heat absorption for Fe_2O_3 particle sizes 30−100 nm, and a 60% increase for 5 μm, while the highest increase was found to be 76.5% for Fe_3O_4 (5 μm). On the other hand, comparing the *SAR* values at a constant magnetic field (*e.g.*, 31.4 mT) for different magnetic particles, the SAR was increased by ∼97.4% for Fe_3O_4 (5 μm) relative to Fe_2O_3 (30 nm), in agreement with the EPR data in Figure 2. As this figure demonstrates, the intensity of the EPR spectrum was the highest for Fe_{20}(D)/13X across the three magnetic fields and decreased as the particle size of Fe_2O_3 decreased. The high *SAR* of the sorbent makes it suitable as a magnetically responsive sorbent for efficient regeneration upon exposure to a magnetic field.

3.2. Unary C_2H_6 and C_2H_4 Adsorption Isotherms. The equilibrium adsorption isotherms of C_2H_6 and C_2H_4 obtained at 25 °C are depicted in Figure 3a,b. As a general trend, the magnetic sorbents exhibited higher affinity for C_2H_4 than for C_2H_6, and the shape of the isotherms was resembled across all the materials, with a steep increase at low pressures followed by a gradual increase at higher pressures. However, the sharpness of the isotherms and the amount of C_2H_6/C_2H_4 adsorbed declined as the particle size of Fe_2O_3 increased, as in Fe_{20}(A−C)/13X sorbents, or when FeO was used as in Fe_{20}(E)/13X. However, when Fe_3O_4 iron oxide was used, such as in Fe_{20}(D)/13X, the sharpness of the isotherms and the amount of C_2H_6/C_2H_4 adsorbed were increased.

The reduction in C_2H_6 and C_2H_4 equilibrium adsorption capacities and the change in the isotherm's shape could be correlated to the reduction in surface area and porosity of the sorbents with larger iron oxide particles [Fe_{20}(A−C)/13X] and with different iron oxides [Fe_{20}(D and E)/13X]. Fe_{20}(A)/13X displayed an equilibrium capacity of 3.22 mmol/g for C_2H_6 and 3.78 mmol/g for C_2H_4 at 1 bar, whereas Fe_{20}(B)/13X and Fe_{20}(C)/13X achieved capacities of 3.19 and 2.79 for C_2H_6 and 3.39 and 3.21 mmol/g for C_2H_4, respectively, as shown in Figure 3a,b. The equilibrium capacities of C_2H_6 and C_2H_4 were increased by 4.7 and 0.62% when Fe_3O_4 was used, as in Fe_{20}(D)/13X, whereas Fe_{20}(B)/13X and Fe_{20}(B)/13X displayed the lowest uptakes on the account of their lowest surface area and porosity, as discussed earlier.

3.3. Magnetic Induction Breakthrough Experiments. The dynamic breakthrough experiments were performed to assess the separation capability of the developed magnetic sorbents using a binary gas mixture of C_2H_4/C_2H_6 with

https://doi.org/10.1021/acssuschemeng.3c01468
ACS Sustainable Chem. Eng. 2023, 11, 8603−8614

Table 3. *SAR* of Magnetic Particles at Different Magnetic Field Strengths

current (mT)	frequency (kHz)	SAR (W/g)					
		Fe_2O_3 (30 nm)	Fe_2O_3 (100 nm)	Fe_2O_3 (5 μm)	Fe_2O_3 (5 μm)/20% FeO	Fe_3O_4 (5 μm)	Fe_2O_3 (ion)/13X (1.4−77 μm)
21.4	215	14.23	20.51	25.11	33.48	214.7	10.46
26.4	215	15.07	24.69	36.83	41.86	694.8	12.55
31.4	215	23.44	27.62	61.53	79.95	916.7	15.90

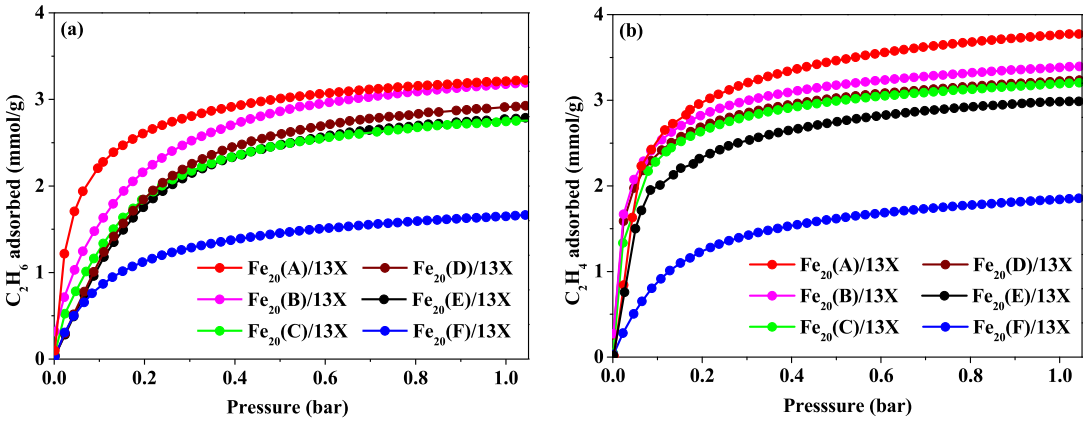

Figure 3. Unary adsorption isotherms of (a) C_2H_6 and (b) C_2H_4 over the Fe_{20}(A−F)/13X sorbents at 25 °C.

equimolar concentrations. The dynamic concentration profiles are depicted in Figure 4, and the corresponding breakthrough data are displayed in Table 4. In agreement with their equilibrium isotherms, all the magnetic sorbents displayed preferential adsorption of C_2H_4 over C_2H_6 with high separation efficiency. Looking at the concentration fronts, the overshoot in the wavefronts of C_2H_6 was caused by the breakthrough of C_2H_4 from the bed outlet. The stronger adsorbate molecules of C_2H_4 displaced the weaker adsorbate molecules of C_2H_6, causing the overshoot above the relative concentration of $C_i/C_0 = 1$. This adsorption mechanism occurs due to the molecular sieving and van der Waals (vdW) forces, where the selective adsorption process is based on the size of the adsorbate molecule and the pore size of the sorbent. C_2H_4 has a smaller kinetic diameter than C_2H_6 (4.163 *vs* 4.443 Å),[34] which allows it to enter the pores of 13X and interact with the sorbent surface through vdW forces (*ca.* π-bond interactions and dipole and quadrupole moments). In contrast, C_2H_6, which has a larger kinetic diameter, is excluded from the smaller pores.[35,36] When binary equilibrium adsorption was attained—which occurs when C_2H_4 approaches the end of the column—both gases returned to their molar feed compositions. Although the uptakes of the C_2H_6 and C_2H_4 were lower over Fe_{20}(F)/13X than over other sorbents, the shape of the front was roughly similar across the sorbents, with slight differences in the sharpness of the desorption profiles of C_2H_6 when the particle size of iron oxide was increased (*i.e.,* it became slightly broader), as in Fe_{20}(C−F)/13X sorbents. These observations were expected based on our previous work, as increasing the iron oxide composition led to different front shapes, which was not the case in this study.[29] It can be reasonably concluded that changing the particle size of iron oxide or using different iron oxides did not severely affect the adsorption kinetics. However, the reduction in C_2H_6 and C_2H_4 uptakes and the difference in breakthrough widths are attributed to the difference in the affinity toward the adsorbates. Indeed, this notation was further supported by the widths of the breakthrough fronts for both gases across the various sorbents. Namely, the breakthrough front widths (*e.g.*, $t_{5\%}$) were reduced by 70 and 60% for ethane and ethylene over Fe_{20}(F)/13X, which had the lowest adsorption uptakes. As a result, both gases broke through earlier than over Fe_{20}(A)/13X, regardless of the particle size. Given that the front's width corresponds directly to the adsorbate diffusion rate, and given that the front's shape was similar across all the sorbents,[37] it was deduced that the diffusion rate was not the driving mechanism for adsorption, and that the variation in breakthrough widths was caused by the difference in the sorbent's affinity toward gases. It is also worth noting here that as the uptake for ethane and ethylene decreased, the selectivity remained roughly constant at 2.44−2.65 (Table 4).

3.4. Effect of Magnetic Induction Heating on the Desorption Profiles. The desorption profiles of C_2H_6 and C_2H_4 along with the temperature profiles (heating and cooling) as a function of time are presented in Figure 5a−d. To assess the effect of iron oxide particle size and phase on the C_2H_6 and C_2H_4 desorption rates, desorption runs were conducted at a fixed magnetic field strength (31.4 mT). As shown in Figure 5d, exposing the adsorption bed to a fixed magnetic field intensity resulted in raising the bed temperature. However, the magnitude of the change varied across the sorbents. The larger particle size of iron oxide led to a greater temperature rise (ΔT), with Fe_{20}(D)/13X displaying the highest ΔT (178 °C), and Fe_{20}(F)/13X displaying the lowest ΔT (27 °C). It is worth noting here that the temperature sensor was limited to 250 °C, so the temperature recording was stopped after exceeding 200 °C. Based on the *SAR* results, such a trend was expected since the specific heat absorption rate increased with iron oxide particle size, with 5 μm particles displaying the highest SAR value.[26] However, this pattern did not hold true for Fe_{20}(F)/13X, despite having a wide particle size range (1.40 to 77 μm). Fe_3O_4 outperformed Fe_2O_3 at the same particle size (5 m) owing to the higher thermal conductivity of Fe_3O_4 which stemmed from its dual ion states

https://doi.org/10.1021/acssuschemeng.3c01468
ACS Sustainable Chem. Eng. 2023, 11, 8603−8614

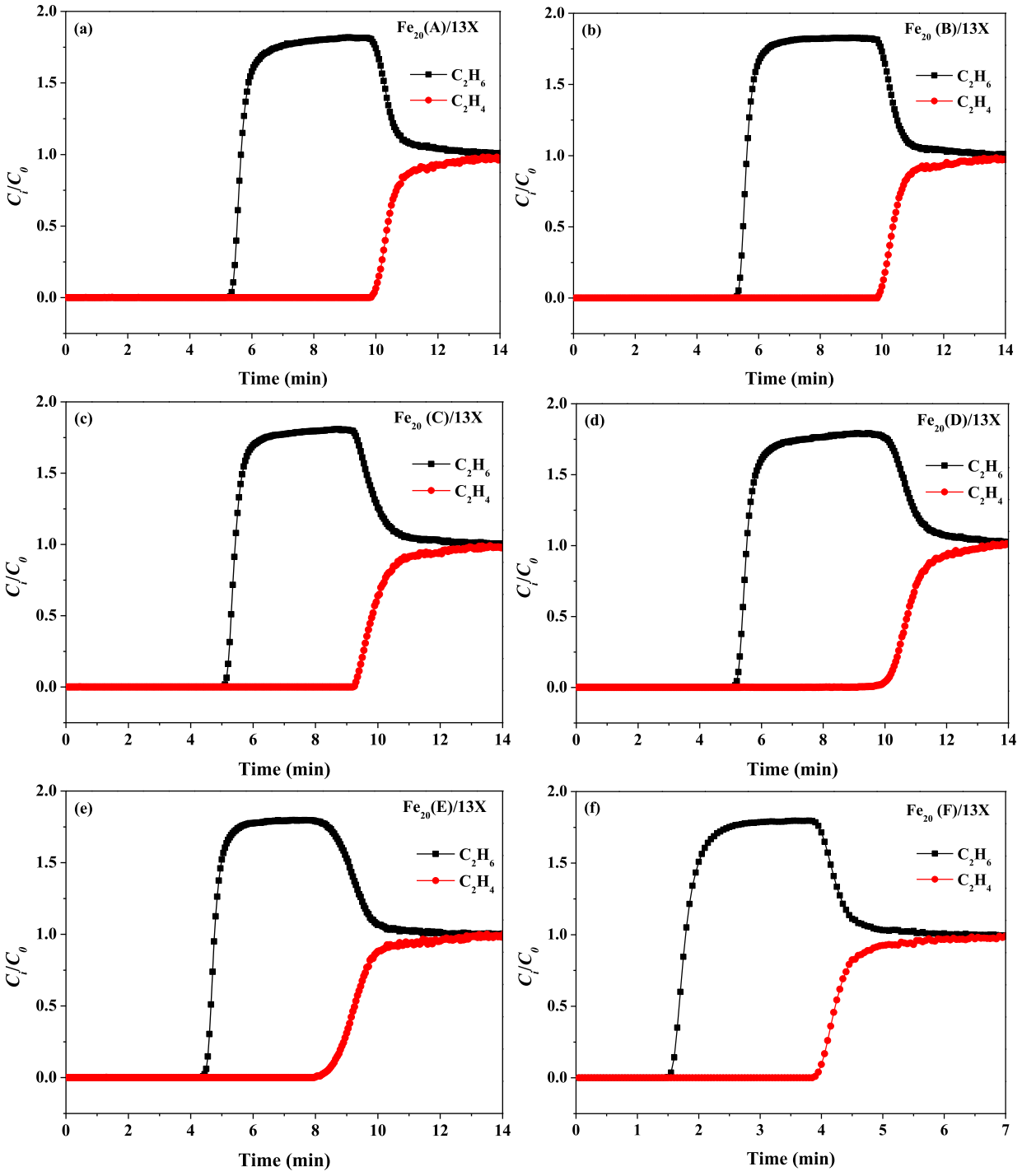

Figure 4. Dynamic concentration profiles for 50/50 vol % C_2H_6/C_2H_4 at 25 °C and 1 bar over (a) Fe_{20}(A)/13X, (b) Fe_{20}(B)/13X, (c) Fe_{20}(C)/13X, (d) Fe_{20}(D)/13X, (e) Fe_{20}(E)/13X, and (f) Fe_{20}(F)/13X.

(Fe^{2+} and Fe^{3+}) within the lattice structure. In the literature, Ji *et al.*[27] demonstrated that Fe_3O_4 has an inverse spinel cubic structure in the form of AB_2O_4, where half of Fe^{3+} occupies the tetrahedral position (A position), while the other half of Fe^{3+} (and Fe^{2+}) locates in the octahedral position (B position). It is very easy for electrons to move between Fe^{2+} and Fe^{3+} in the B position, and under high electric current frequencies, Fe^{2+} can be easily polarized and induce high electromagnetic waves.[28,38]

As a result of different responses to the magnetic field during desorption step, ethane and ethylene desorption rates varied accordingly. In Fe_{20}(A–D)/13X sorbents, a gradual increase in the outlet mole fraction of both gases was observed, whereas in the case of Fe_{20}(E)/13X and Fe_{20}(F)/13X, a decline in the outlet mole fraction was noted (Figure 5a,b). The average desorption rates of ethylene at 31.4 mT were increased from 0.07 to 0.22 and 0.69 mmol/g·min for Fe_{20}(A)/13X, Fe_{20}(B)/13X, Fe_{20}(C)/13X, and Fe_{20}(D)/13X, respectively, then reduced to 0.21 and 0.06 mmol/g·min for Fe_{20}(E)/13X and Fe_{20}(F)/13X, respectively, as shown in Table 5. Notably, Fe_{20}(D)/13X demonstrated the highest desorption rate (0.69 mmol/g·min) than Fe_{20}(A)/13X and Fe_{20}(B)/13X, owing to its excellent magnetic properties and low ethane and ethylene

https://doi.org/10.1021/acssuschemeng.3c01468
ACS Sustainable Chem. Eng. 2023, 11, 8603−8614

Table 4. Dynamic Adsorption Data for Binary Runs at 25 °C and 1 bar for Fe_{20}(A–F)/13X Sorbents

breakthrough parameter	$t_{ads,5\%}$ (min)	$t_{ads,50\%}$ (min)	$t_{ads,95\%}$ (min)	breakthrough width (min)	$q_{ads,5\%}$ (mmol/g)	$q_{ads,50\%}$ (mmol/g)	$q_{ads,95\%}$ (mmol/g)	selectivity (C_2H_4/C_2H_6)
				C_2H_6				
Fe_{20}(A)/13X	5.32	5.43	5.59	0.27	0.84	1.07	1.16	2.59
Fe_{20}(B)/13X	5.30	5.42	5.56	0.26	0.82	1.00	1.15	2.61
Fe_{20}(C)/13X	5.08	5.23	5.38	0.30	0.81	0.95	1.07	2.57
Fe_{20}(D)/13X	5.17	5.33	5.47	0.30	0.81	0.94	1.10	2.65
Fe_{20}(E)/13X	4.42	4.58	4.70	0.28	0.56	0.69	0.97	2.58
Fe_{20}(F)/13X	1.54	1.64	1.72	0.18	0.33	0.45	0.61	2.44
				C_2H_4				
Fe_{20}(A)/13X	9.92	10.30	12.50	2.65	2.47	2.56	3.01	
Fe_{20}(B)/13X	9.91	10.30	12.90	2.99	2.30	2.52	3.00	
Fe_{20}(C)/13X	9.27	9.79	12.00	2.78	2.26	2.29	2.75	
Fe_{20}(D)/13X	10.0	10.70	13.00	3.04	2.39	2.46	2.91	
Fe_{20}(E)/13X	8.35	9.20	11.30	3.00	2.04	2.07	2.50	
Fe_{20}(F)/13X	3.93	4.17	5.47	1.54	0.32	1.08	1.49	

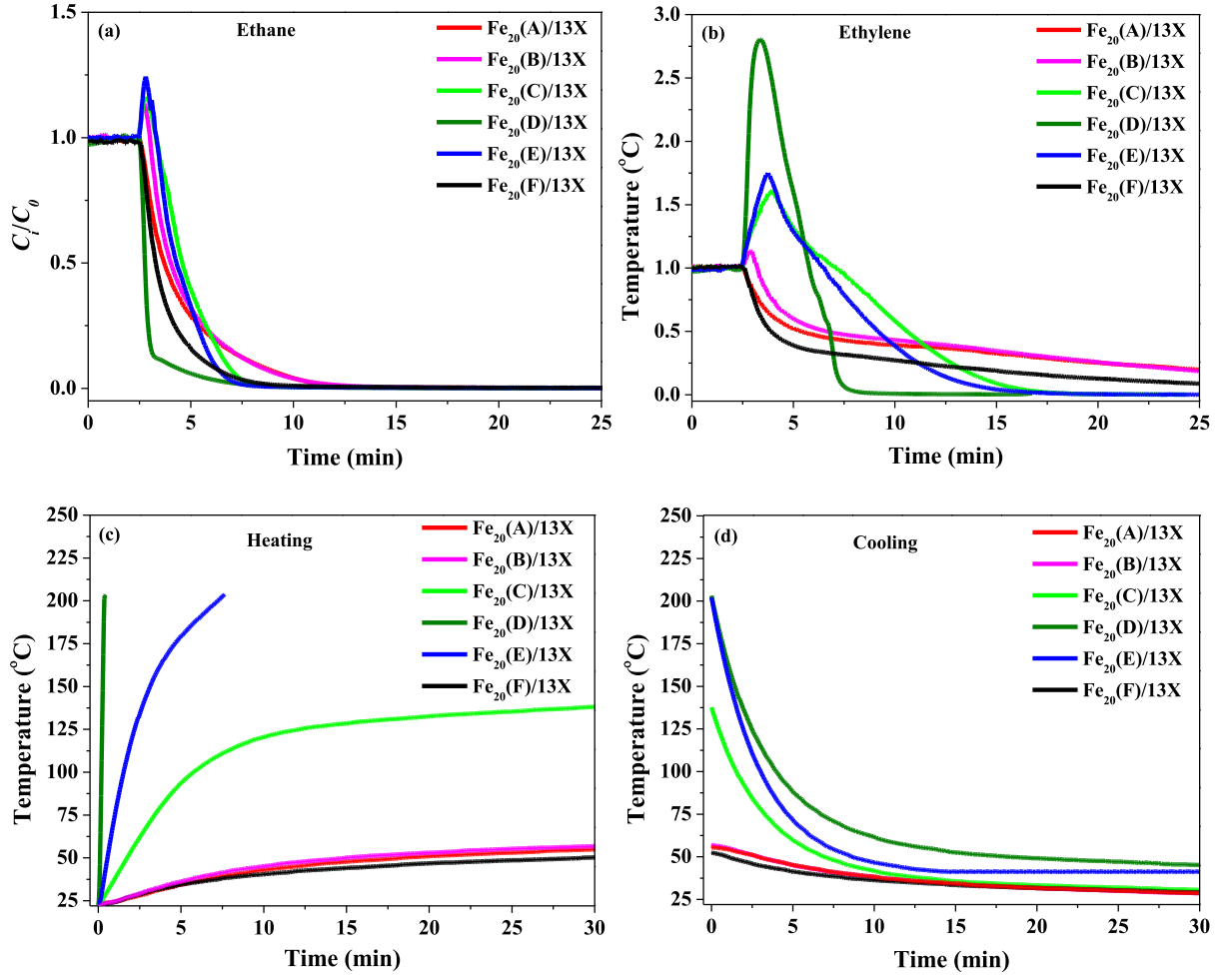

Figure 5. Desorption profiles of (a) C_2H_6 and (b) C_2H_4 at 31.4 mT over Fe_{20}(A–F)/13X and temperature profiles during (c) heating and (d) cooling steps.

uptakes. Induction heating depends on three primary factors to control desorption rate: desorption time, gas uptake, and the *SAR*.[21] During desorption, some energy is consumed by desorption enthalpy, while the rest dissipates into the gas stream.[21,39] With a larger iron oxide particle size, the heat intensity increases, and more energy is absorbed to heat the bed, especially given that 13X has a low thermal conductivity.[24] As noted before, Fe_3O_4 has a unique lattice structure with dual ion states, moderate adsorption capacity, and a large particle size (5 μm), which makes Fe_{20}(D)/13X the most efficient magnetic sorbent with the fastest desorption rates of both C_2H_6 and C_2H_4. A similar trend was observed for ethane, except over Fe_{20}(A)/13X and Fe_{20}(B)/13X (Table 5). The temperature profiles (Figure 5d) during cooling step were recorded as well, and as expected, the results showed that as

https://doi.org/10.1021/acssuschemeng.3c01468
ACS Sustainable Chem. Eng. 2023, 11, 8603–8614

Table 5. Dynamic Desorption Data (Average Values) for Binary Runs over Magnetic Sorbents at 21.4, 26.4, and 31.4 mT

sorbent	$t_{des,(C_2H_6)}$ (s)	$t_{des,(C_2H_4)}$ (s)	desorption rate (r_{des}), C_2H_6 (mmol/g·min)	desorption rate (r_{des}), C_2H_4 (mmol/g·min)
		21.4 mT		
Fe_{20}(A)/13X	11.3	86.01	0.12	0.04
Fe_{20}(B)/13X	12.4	90.50	0.10	0.04
Fe_{20}(C)/13X	6.60	28.65	0.18	0.12
Fe_{20}(D)/13X	6.10	8.780	0.20	0.41
Fe_{20}(E)/13X	4.71	22.90	0.20	0.14
Fe_{20}(F)/13X	8.25	47.80	0.09	0.04
		26.4 mT		
Fe_{20}(A)/13X	10.1	78.55	0.13	0.05
Fe_{20}(B)/13X	11.5	70.45	0.11	0.05
Fe_{20}(C)/13X	5.75	27.10	0.21	0.13
Fe_{20}(D)/13X	5.95	6.850	0.21	0.52
Fe_{20}(E)/13X	4.70	22.80	0.20	0.14
Fe_{20}(F)/13X	7.75	43.45	0.10	0.05
		31.4 mT		
Fe_{20}(A)/13X	9.75	51.70	0.13	0.07
Fe_{20}(B)/13X	9.70	51.40	0.13	0.07
Fe_{20}(C)/13X	5.55	15.80	0.22	0.22
Fe_{20}(D)/13X	5.05	5.150	0.25	0.69
Fe_{20}(E)/13X	4.68	15.30	0.21	0.21
Fe_{20}(F)/13X	7.64	37.85	0.10	0.06

the desorption temperature was higher, a longer time was required to cool down the bed back to room temperature.

3.5. Effect of Magnetic Field Strength. To assess the effect of magnetic field strength on the desorption performance of the magnetic sorbents, desorption profiles of C_2H_4 and C_2H_6 were collected at three different field intensities, and the results are shown in Figure 6a–c [Fe_{20}(D)/13X] and Figures S2–S6. According to Table 5, increasing the magnetic field strength from 21.4 to 31.4 mT improved the ethylene/ethane desorption rates for all the sorbents. For example, the desorption rate of ethylene over Fe_{20}(D)/13X increased from 0.41 to 0.52 and 0.69 mmol/g·min when field intensity increased from 21.4 to 26.4 and 31.4 mT, respectively. Hence, with micro-sized iron oxide, more energy was absorbed to warm up the adsorption bed, leading to an increased sorbent's temperature, and thereby promoting the desorption rate of the gaseous species. Similar enhancement in desorption rate was observed for Fe_{20}(C)/13X and Fe_{20}(D)/13X, albeit the enhancement was the highest for Fe_{20}(D)/13X at 0.69 mmol/g·min. Additionally, for Fe_{20}(D)/13X, ethylene desorption was higher than that of ethane in all three cases, which gave rise to lower ethane desorption rates. For this material, the rate of desorption increased with field intensity and was estimated to be 40% for ethylene and 20% for ethane. This trend may not be observed in all sorbents, which can be explained by taking into account the difference in their desorption performance in terms of gas uptake, time, and absorption heat, as these factors are largely responsible for the magnitude of the desorption rate.

3.6. Thermal Heating *versus* Magnetic Induction. As a means of assessing the effectiveness of induction heating, desorption experiments on the most effective sorbent [Fe_{20}(D)/13X] were carried out at 200 °C under conventional thermal heating, and the results were compared with those under magnetic induction at 21.4 mT, as shown in Figure 7a–d. As clearly evident, magnetic induction gave rise to a 68% faster heating than conventional thermal mode (Figure 7a), thereby leading to different desorption profiles (Figure 7c,d). With induction heating, the concentration fronts of both species were spiked earlier than those under conventional heating. This can be attributed to the direct transfer of energy from the magnetic field to the Fe_3O_4 particles, thereby causing rapid sorbent regeneration. In conventional heating, the column wall and sorbent must be heated simultaneously, which results in a longer heating time.[26] As a result of this remarkable feature of induction heating, ethane and ethylene desorption rates were much faster at 0.41 and 0.20 mmol/g·min, respectively, compared to 0.17 and 0.08 mmol/g·min in the case of conventional heating, as shown in Figure 7c,d.

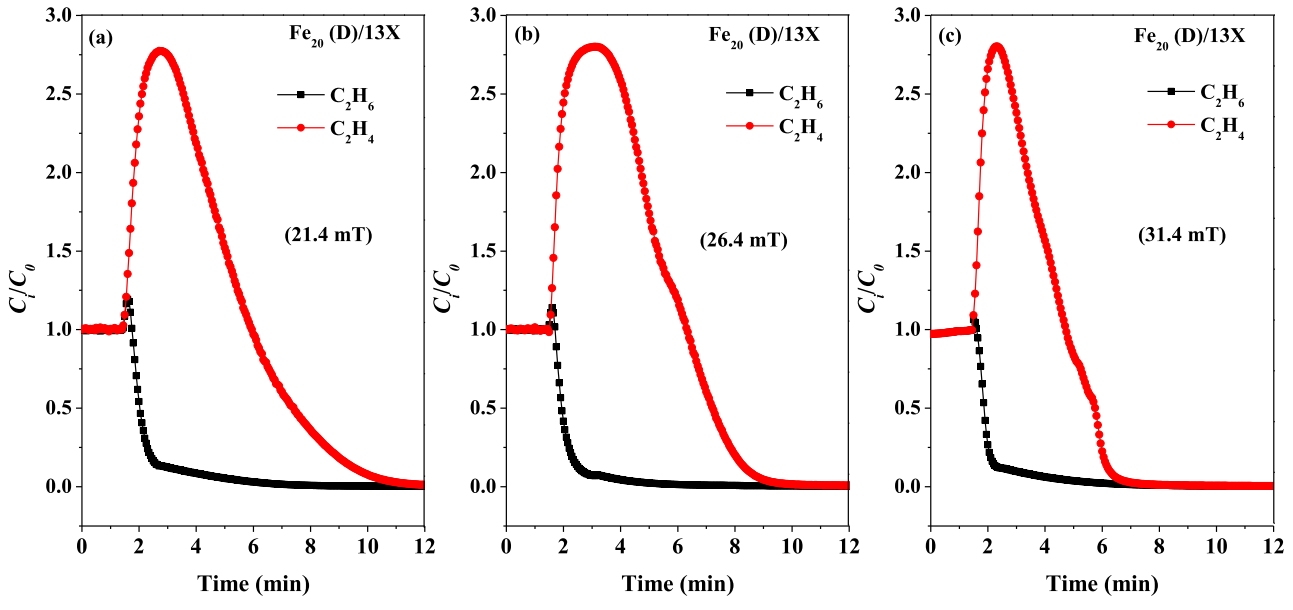

Figure 6. Desorption profiles of C_2H_6 and C_2H_4 at (a) 21.4, (b) 26.4, and (c) 31.4 mT field strengths over Fe_{20}(D)/13X.

https://doi.org/10.1021/acssuschemeng.3c01468
ACS Sustainable Chem. Eng. 2023, 11, 8603–8614

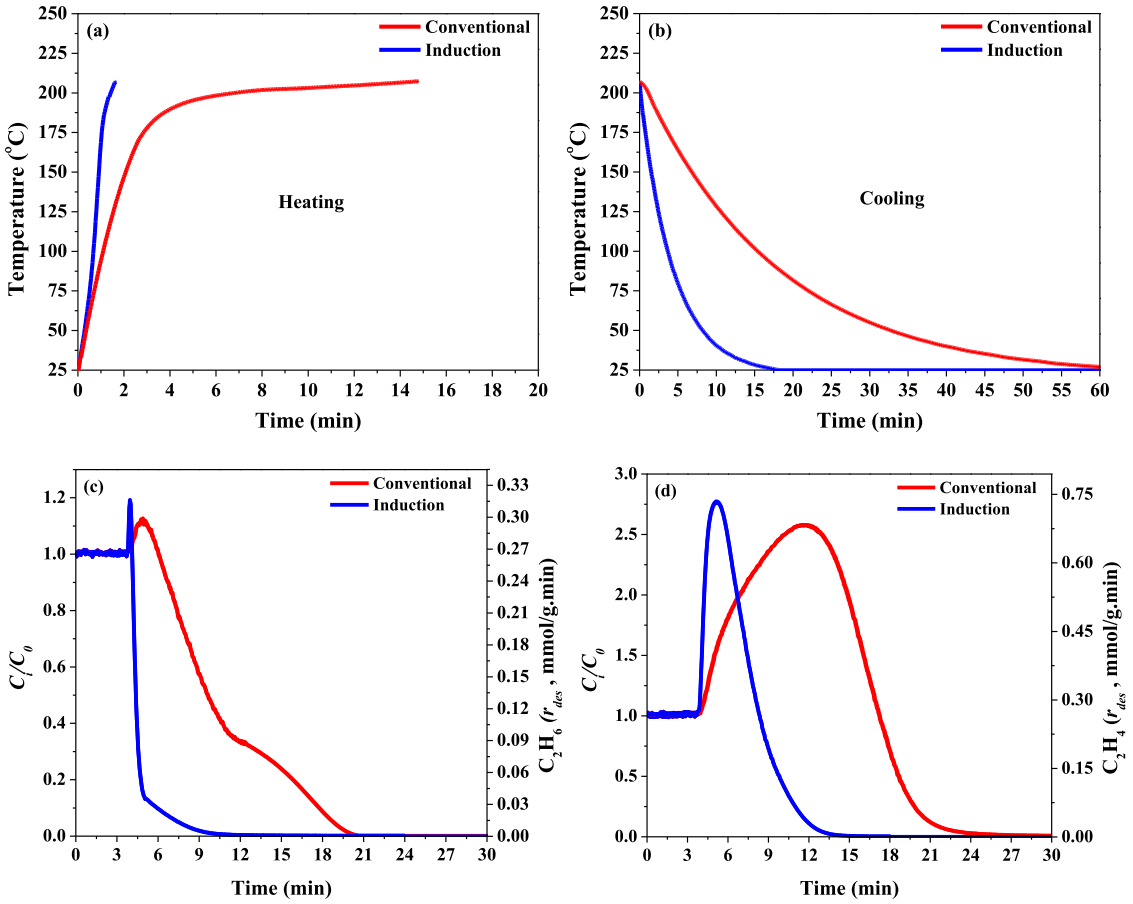

Figure 7. Comparison between induction and conventional heating and their effect on desorption and cooling rates using Fe_{20}(D)/13X (a,b) heating and cooling profiles; (c,d) ethane and ethylene relative concentrations and desorption rates as a function of time.

Moreover, indirect heating was superior to conventional heating during cooling step, as shown in Figure 7b, by displayinga much faster cooling rate (*ca.* 71%). Thermal desorption involves heating almost the entire column to regenerate the sorbent, resulting in prolonged cooling times. Using induction heating, on the other hand, does not require conduction heating since the magnetic field targets only the sorbent, and the heat is confined to a small area (adsorption bed) within the induction coil, making the cooling step faster.[29] The cooling rate—when using conventional heating method—was 3.43 °C/min, which increased to 11.77 °C/min when induction heating was used (Figure 7b). It is advantageous from a process standpoint to have a faster cooling rate since cooling is typically the limiting step for swing adsorption processes, as a dramatic reduction in the cycle step will improve adsorption process efficiency with a smaller column size. Compared to the conventional heating method, induction heating improved the cooling rate significantly, making it a promising option for sorbent regeneration in the adsorptive separation process of paraffins and olefins.

3.7. Cyclic MISA Experiments. The assessment of sorbents performance under cyclic conditions is crucial to determine their effectiveness for practical applications. In this study, we investigated the cyclic MISA performance of Fe_{20}(D)/13X, as the best performing sorbent, using a binary feed mixture of C_2H_4/C_2H_6 through five adsorption–desorption cycles at 25 °C and 1 bar (adsorption) and 31.4 mT magnetic field strength (desorption). The corresponding results presented in Figure 8 demonstrate that the adsorption

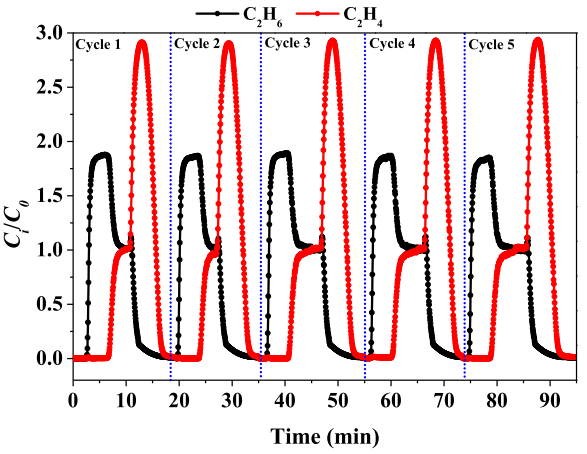

Figure 8. Cyclic MISA experiments over Fe_{20}(D)/13X sorbent at 25 °C, 1 bar (adsorption), and 31.4 mT (desorption).

efficiencies and desorption rates remained unchanged across the five cycles without any reductions in the amount of C_2H_6 and C_2H_4 adsorbed or desorbed, indicating excellent durability of the Fe_{20}(D)/13X sorbent. The remarkable stability observed in the cyclic runs suggests that Fe_{20}(D)/13X has a potential to be an efficient sorbent for practical applications in the MISA process.

3.8. Estimation of Regeneration Energy Requirements. The regeneration energy requirements of the MISA process with the Fe_{20}(D)/13X sorbent were also determined in

https://doi.org/10.1021/acssuschemeng.3c01468
ACS Sustainable Chem. Eng. 2023, 11, 8603−8614

this study. A key factor determining the feasibility of sorbents in gas separations is the regeneration energy (Q, MJ/kg), which refers to the energy needed to desorb the adsorbates and reverse the adsorption process.[40] In order to estimate the regeneration energy, the heat of adsorption (ΔH_{st}, kJ/mol) and specific heat capacity (C_p, J/g·°C) of Fe_{20}(D)/13X were determined *via* isotherm measurements and DSC experiments, respectively, as detailed in the Supporting Information, following methods reported in the literature.[19,24,25,36] The resulting data for ethane and ethylene are presented in Tables 6 and 7, respectively.

Table 6. Regeneration Energy Calculations for Ethane Desorption Using Fe_{20}(D)/13X at Different Magnetic Fields (mT)

	magnetic strength (mT)		
parameter	21.4 mT	26.4 mT	31.4 mT
m_{ads} (g)	0.10	0.10	0.10
frequency (kHz)	215	215	215
m_s (g)	0.02	0.02	0.02
SAR (W/g)	214.7	694.8	916.7
ΔH_{st} (kJ/mol)	30.40	30.40	30.40
Δq_{gas} (mmol)	0.144	0.147	0.155
t_{des} (s)	366	357	303
m_{gas} (g)	0.00879	0.00879	0.00879
C_p (J/g·°C)	1.50	1.50	1.50
ΔT (°C)	154	161	178
Q (MJ/kg)	3.13	3.26	3.57

Table 7. Regeneration Energy Calculations for Ethylene Desorption Using Fe_{20}(D)/13X at Different Magnetic Fields (mT)

	magnetic strength (mT)		
parameter	21.4 mT	26.4 mT	31.4 mT
m_{ads} (g)	0.10	0.10	0.10
frequency (kHz)	215	215	215
m_s (g)	0.02	0.02	0.02
SAR (W/g)	214.7	694.8	916.7
ΔH_{st} (kJ/mol)	45	45	45
Δq_{gas} (mmol)	0.169	0.176	0.183
t_{des} (s)	526	411	309
m_{gas} (g)	0.00896	0.00896	0.00896
C_p (J/g·°C)	1.50	1.50	1.50
ΔT (°C)	154	161	178
Q (MJ/kg)	3.43	3.58	3.90

Another parameter that has a significant impact on the regeneration energy of sorbents is the working capacity (Δq_{gas}, mmol). The working capacity of a material refers to the difference between the amounts adsorbed and desorbed under specific temperature and pressure conditions. This is an important factor in determining the efficacy of the material in gas separation and purification applications. A material with a high working capacity and low regeneration energy would be preferable, as it would allow for efficient adsorption and desorption of the adsorbate with minimal energy input.[41] The working capacity was estimated by measuring the difference between the gas adsorption capacities of ethane or ethylene at 0.15 bar and 25 °C, and at the desorption temperature and 1 bar (Figure S7c,d).[24] The desorption temperatures used in calculations were 154, 161, and 178 °C, which corresponded to the magnetic fields of 21.4, 26.4, and 31.4 mT, respectively. As the data in Tables 6 and 7 indicate, the energy needed for ethylene desorption was higher than that for ethane across all magnetic fields. Despite ethane exhibiting a lower working capacity, these findings were expected due to the higher isosteric heat of adsorption for ethylene compared to that for ethane (30.4 *vs* 45.0 kJ/mol). Moreover, comparing the energy required for gas desorption with previously reported data in the literature (Table S4), the Q values for ethane and ethylene were lower than the reported values for CO_2 release over $MgFe_2O_4$@UiO-66.[24] This reduction in energy requirement can be attributed to the high magnetic responsiveness of Fe_3O_4 in Fe_{20}(D)/13X, as discussed earlier, resulting in a 52.42% decrease in Q value at 21.4 mT, relative to that for the above magnetic MOF.

In comparison to previously reported studies (Table S4) on CO_2 release using induction heating, the developed magnetic sorbent Fe_{20}(D)/13X exhibited outstanding performance. Fe_{20}(D)/13X demonstrated a higher *SAR* compared to that for Fe_{20}/13X extrudates and $MgFe_2O_4$@UiO-66 at a comparable magnetic strength of approximately 21.4 mT. Specifically, Fe_{20}(D)/13X had a *SAR* of 214.7 mT, whereas Fe_{20}/13X and $MgFe_2O_4$@UiO-66 exhibited *SAR* values of 137.9 and 32.4, respectively.[21,24] Additionally, the *SAR* of Fe_{20}(D)/13X was notably higher than what was previously reported in our own work.[29] The variation in *SAR* values among the magnetic sorbents developed in this study and other studies can be correlated to the factors such as different iron oxide phases, particle sizes, and synthesis methods utilized. In terms of desorption rate or gas release capability, the *SAR* of the sorbent and its adsorption capacity play a significant role. Therefore, the desorption rate is expected to vary with the *SAR* and adsorption capacity values, as shown in Table S4. On the other hand, Fe_{20}(D)/13X exhibited favorable adsorption performance compared to other non-magnetic sorbents reported for ethylene/ethane separation by adsorption. The experimental ethylene/ethane selectivity of Fe_{20}(D)/13X fell within the expected range for light olefin/paraffin separation, as demonstrated in Table S5.[42,43]

4. CONCLUSIONS

In this study, six magnetic sorbents comprising iron oxide and 13X zeolite with varied particle size and iron oxide phase were prepared and assessed in ethylene/ethane separation *via* magnetic induction heating. The results indicated that the generated heat during desorption is directly correlated to the particle size of iron oxide and interfacial polarization, which is mainly caused by the lattice dislocations in the structure of iron oxide. The enhanced magnetic responsiveness of Fe_3O_4 relative to FeO and Fe_2O_3 was attributed to its dual ion states of Fe^{2+} and Fe^{3+}, which increases electron vibrations during exposure to a magnetic stimulus, thus rendering Fe_{20}(D)/13X as the best performing magnetic sorbent. Fe_{20}(D)/13X displayed 93.3% higher absorption heat compared to its counterpart Fe_{20}(C)/13X at 31.4 mT, resulting in the highest ethylene desorption rate of 0.69 mmol/g·min. Furthermore, a comparison between conventional and induction heating methods in the regeneration of sorbents highlighted the advantages of induction heating in regenerating the sorbent at a faster rate (58.5%) than the thermal heating mode. Furthermore, it was observed that the sorbent exhibited high durability, maintaining its adsorption−desorption performance across five consecutive cycles in the MISA process. Overall,

https://doi.org/10.1021/acssuschemeng.3c01468
ACS Sustainable Chem. Eng. 2023, 11, 8603−8614

these findings indicate that Fe_3O_4/13X is a highly effective magnetic sorbent for olefin/paraffin separation under magnetic-induced swing adsorption.

■ ASSOCIATED CONTENT

Supporting Information

The Supporting Information is available free of charge at https://pubs.acs.org/doi/10.1021/acssuschemeng.3c01468.

Specific heat absorption rate (SAR) calculations; temperature profiles of iron oxides dispersed in water; desorption profiles of C_2H_6 and C_2H_4; unary adsorption isotherms of C_2H_6 and C_2H_4 using the Fe20(D)/13X sorbent at different temperatures; heat of adsorption and regeneration energy calculations; heat flow and heat capacity as a function of temperature measured by DSC; SAR data for different iron oxides; and comparison of desorption rates, SAR, and regeneration energy values with reported data (PDF)

■ AUTHOR INFORMATION

Corresponding Author

Fateme Rezaei − *Linda and Bipin Doshi Department of Chemical & Biochemical Engineering, Missouri University of Science and Technology, Rolla, Missouri 65409, United States;* orcid.org/0000-0002-4214-4235; Email: rezaeif@mst.edu

Authors

Khaled Baamran − *Linda and Bipin Doshi Department of Chemical & Biochemical Engineering, Missouri University of Science and Technology, Rolla, Missouri 65409, United States*

Ali A. Rownaghi − *Department of Chemistry, Cleveland State University, Cleveland, Ohio 44115, United States;* orcid.org/0000-0001-5228-5624

Complete contact information is available at: https://pubs.acs.org/10.1021/acssuschemeng.3c01468

Notes

The authors declare no competing financial interest.

■ ACKNOWLEDGMENTS

The involvement of A.A.R. in this work was sponsored by the National Science Foundation (NSF CBET-2019350).

■ REFERENCES

(1) Chen, C.; Wei, Z.; Pham, T.; Lan, P. C.; Zhang, L.; Forrest, K. A.; Chen, S.; Al-Enizi, A. M.; Nafady, A.; Su, C.; et al. Nanospace Engineering of Metal−Organic Frameworks through Dynamic Spacer Installation of Multifunctionalities for Efficient Separation of Ethane from Ethane/Ethylene Mixtures. *Angew. Chem., Int. Ed.* **2021**, *60*, 9680−9685.

(2) Kang, M.; Yoon, S.; Ga, S.; Kang, D. W.; Han, S.; Choe, J. H.; Kim, H.; Kim, D. W.; Chung, Y. G.; Hong, C. S. High-Throughput Discovery of $Ni(IN)_2$ for Ethane/Ethylene Separation. *Adv. Sci.* **2021**, *8*, 2004940.

(3) Baamran, K.; Lawson, S.; Rownaghi, A. A.; Rezaei, F. Process Evaluation and Kinetic Analysis of 3D-Printed Monoliths Comprised of CaO and Cr/H-ZSM-5 in Combined CO_2 Capture-C_2H_6 Oxidative Dehydrogenation to C_2H_4. *Chem. Eng. J.* **2022**, *435*, 134706.

(4) Lawson, S.; Baamran, K.; Newport, K.; Rezaei, F.; Rownaghi, A. A. Formulation and Processing of Dual Functional Adsorbent/Catalyst Structured Monoliths Using an Additively Manufactured Contactor for Direct Capture/Conversion of CO_2 with Cogeneration of Ethylene. *Chem. Eng. J.* **2022**, *431*, 133224.

(5) Baamran, K.; Rownaghi, A. A.; Rezaei, F. Direct Synthesis of Ethylene and Hydrogen from CO_2 and Ethane over a Bifunctional Structured CaO/Cr_2O_3-V_2O_5/ZSM-5 Adsorbent/Catalyst Monolith. *ACS Sustainable Chem. Eng.* **2022**, *11*, 1006−1018.

(6) Li, L.; Lin, R.-B.; Krishna, R.; Li, H.; Xiang, S.; Wu, H.; Li, J.; Zhou, W.; Chen, B. Ethane/Ethylene Separation in a Metal-Organic Framework with Iron-Peroxo Sites. *Science* **2018**, *362*, 443−446.

(7) Zhou, P.; Yue, L.; Wang, X.; Fan, L.; Chen, D.-L.; He, Y. Improving Ethane/Ethylene Separation Performance of Isoreticular Metal−Organic Frameworks via Substituent Engineering. *ACS Appl. Mater. Interfaces* **2021**, *13*, 54059−54068.

(8) Al-Naddaf, Q.; Rownaghi, A. A.; Rezaei, F. Multicomponent adsorptive separation of CO_2, CO, CH_4, N_2, and H_2 over core-shell zeolite-5A@MOF-74 composite adsorbents. *Chem. Eng. J.* **2020**, *384*, 123251.

(9) Yin, Y.; Zhang, Z.; Xu, C.; Wu, H.; Shi, L.; Wang, S.; Xu, X.; Yuan, A.; Wang, S.; Sun, H. Confinement of Ag(I) Sites within MIL-101 for Robust Ethylene/Ethane Separation. *ACS Sustainable Chem. Eng.* **2019**, *8*, 823−830.

(10) Thakkar, H.; Eastman, S.; Al-Naddaf, Q.; Rownaghi, A. A.; Rezaei, F. 3D-Printed Metal−Organic Framework Monoliths for Gas Adsorption Processes. *ACS Appl. Mater. Interfaces* **2017**, *9*, 35908−35916.

(11) Liu, Z.; Qiu, W.; Quan, W.; Koros, W. J. Advanced carbon molecular sieve membranes derived from molecularly engineered cross-linkable copolyimide for gas separations. *Nat. Mater.* **2023**, *22*, 109−116.

(12) Thakkar, H.; Al-Naddaf, Q.; Legion, N.; Hovis, M.; Krishnamurthy, A.; Rownaghi, A. A.; Rezaei, F. Adsorption of Ethane and Ethylene over 3D-Printed Ethane-Selective Monoliths. *ACS Sustainable Chem. Eng.* **2018**, *6*, 15228−15237.

(13) Liao, P.-Q.; Zhang, W. X.; Zhang, J. P.; Chen, X. M. Efficient purification of ethene by an ethane-trapping metal-organic framework. *Nat. Commun.* **2015**, *6*, 8697.

(14) Adil, K.; Belmabkhout, Y.; Pillai, R. S.; Cadiau, A.; Bhatt, P. M.; Assen, A. H.; Maurin, G.; Eddaoudi, M. Gas/Vapour Separation Using Ultra-Microporous Metal−Organic Frameworks: Insights into the Structure/Separation Relationship. *Chem. Soc. Rev.* **2017**, *46*, 3402−3430.

(15) Chu, Y.-H.; Yancey, D.; Xu, L.; Martinez, M.; Brayden, M.; Koros, W. Iron-containing carbon molecular sieve membranes for advanced olefin/paraffin separations. *J. Membr. Sci.* **2018**, *548*, 609−620.

(16) Gelles, T.; Rownaghi, A. A.; Rezaei, F. Diffusion Kinetics of CO_2, CH_4, and their Binary Mixtures in Porous Organic Cage CC_3. *J. Phys. Chem. C* **2019**, *123*, 24172−24180.

(17) Chronopoulos, T.; Fernandez-Diez, Y.; Maroto-Valer, M. M.; Ocone, R.; Reay, D. A. CO_2 Desorption via Microwave Heating for Post-Combustion Carbon Capture. *Microporous Mesoporous Mater.* **2014**, *197*, 288−290.

(18) Gomez-Rueda, Y.; Verougstraete, B.; Ranga, C.; Perez-Botella, E.; Reniers, F.; Denayer, J. F. M. Rapid Temperature Swing Adsorption Using Microwave Regeneration for Carbon Capture. *Chem. Eng. J.* **2022**, *446*, 137345.

(19) Lawson, S.; Li, X.; Thakkar, H.; Rownaghi, A. A.; Rezaei, F. Recent Advances in 3D Printing of Structured Materials for Adsorption and Catalysis Applications. *Chem. Rev.* **2021**, *121*, 6246−6291.

(20) Schoukens, M.; Gholami, M.; Baron, G. V.; Van Assche, T.; Denayer, J. F. M. Hybrid Induction Vacuum Swing Adsorption, a Rapid and Fully Electrified Carbon Capture Process. *Chem. Eng. J.* **2023**, *459*, 141587.

(21) Gholami, M.; Verougstraete, B.; Vanoudenhoven, R.; Baron, G. V.; Van Assche, T.; Denayer, J. F. M. Induction Heating as an Alternative Electrified Heating Method for Carbon Capture Process. *Chem. Eng. J.* **2022**, *431*, 133380.

(22) Grande, C. A.; Ribeiro, R. P. L.; Oliveira, E. L. G.; Rodrigues, A. E. Electric Swing Adsorption as Emerging CO_2 Capture Technique. *Energy Procedia* **2009**, *1*, 1219−1225.

(23) Mocho, P.; Le Cloirec, P. Regeneration of Granular Activated Carbon by Inductive Heating-Application in the Elimination and Recycling of Air-Born Solvents. *Stud. Environ. Sci.* **1994**, *61*, 251−259.
(24) Sadiq, M. M.; Li, H.; Hill, A. J.; Falcaro, P.; Hill, M. R.; Suzuki, K. Magnetic Induction Swing Adsorption: An Energy Efficient Route to Porous Adsorbent Regeneration. *Chem. Mater.* **2016**, *28*, 6219−6226.
(25) Sadiq, M. M.; Konstas, K.; Falcaro, P.; Hill, A. J.; Suzuki, K.; Hill, M. R. Engineered Porous Nanocomposites That Deliver Remarkably Low Carbon Capture Energy Costs. *Cell Rep. Phys. Sci.* **2020**, *1*, 100070.
(26) Newport, K.; Baamran, K.; Rownaghi, A. A.; Rezaei, F. Magnetic-Field Assisted Gas Desorption from Fe_2O_3/Zeolite 13X Sorbent Monoliths for Biogas Upgrading. *Ind. Eng. Chem. Res.* **2022**, *61*, 18843−18853.
(27) Ji, J.; Huang, Y.; Yin, J.; Zhao, X.; Cheng, X.; He, S.; Li, X.; He, J.; Liu, J. Synthesis and Electromagnetic and Microwave Absorption Properties of Monodispersive Fe_3O_4/α-Fe_2O_3 Composites. *ACS Appl. Nano Mater.* **2018**, *1*, 3935−3944.
(28) Seo, H.; Ogata, M.; Fukuyama, H. Theory of the Verwey Transition in Fe_3O_4. *Phys. B* **2003**, *329*−*333*, 932−933.
(29) Baamran, K.; Newport, K.; Rownaghi, A. A.; Rezaei, F. Development and Assessment of Magnetic Fe_2O_3@MOF-74 Composite Sorbents for Ethylene/Ethane Separation. *Chem. Eng. J.* **2023**, *451*, 139006.
(30) Ambroz, F.; Macdonald, T. J.; Martis, V.; Parkin, I. P. Evaluation of the BET Theory for the Characterization of Meso and Microporous MOFs. *Small Methods* **2018**, *2*, 1800173.
(31) Thommes, M.; Kaneko, K.; Neimark, A. V.; Olivier, J. P.; Rodriguez-Reinoso, F.; Rouquerol, J.; Sing, K. S. W. Physisorption of Gases, with Special Reference to the Evaluation of Surface Area and Pore Size Distribution (IUPAC Technical Report). *Pure Appl. Chem.* **2015**, *87*, 1051−1069.
(32) Xia, K.; Gao, Q.; Jiang, J.; Hu, J. Hierarchical Porous Carbons with Controlled Micropores and Mesopores for Supercapacitor Electrode Materials. *Carbon* **2008**, *46*, 1718−1726.
(33) Abdellahi, M.; Tajally, M.; Mirzaee, O. The Effect of the Particle Size on the Heating and Drug Release Potential of the Magnetic Nanoparticles in a Novel Point of View. *J. Magn. Magn. Mater.* **2021**, *530*, 167938.
(34) Wu, H.; Chen, Y.; Lv, D.; Shi, R.; Chen, Y.; Li, Z.; Xia, Q. An Indium-Based Ethane-Trapping MOF for Efficient Selective Separation of C_2H_6/C_2H_4 Mixture. *Sep. Purif. Technol.* **2019**, *212*, 51−56.
(35) Anwar, F.; Khaleel, M.; Wang, K.; Karanikolos, G. N. Selectivity Tuning of Adsorbents for Ethane/Ethylene Separation: A Review. *Ind. Eng. Chem. Res.* **2022**, *61*, 12269−12293.
(36) Narin, G.; Martins, V. F. D.; Campo, M.; Ribeiro, A. M.; Ferreira, A.; Santos, J. C.; Schumann, K.; Rodrigues, A. E. Light Olefins/Paraffins Separation with 13X Zeolite Binderless Beads. *Sep. Purif. Technol.* **2014**, *133*, 452−475.
(37) Baamran, K.; Al-Naddaf, Q.; Lawson, S.; Ali Rownaghi, A.; Rezaei, F. Kinetic Process Assessment of H_2 Purification over Highly Porous Carbon Sorbents under Multicomponent Feed Conditions. *Sep. Purif. Technol.* **2023**, *306*, 122695.
(38) Yin, J.-X.; Liu, Z.-G.; Wu, S.-F.; Wang, W.-H.; Kong, W.-D.; Richard, P.; Yan, L.; Ding, H. Unconventional Magnetization of Fe_3O_4 Thin Film Grown on Amorphous SiO_2 Substrate. *AIP Adv.* **2016**, *6*, 065111.
(39) Lin, X.; Shao, B.; Zhu, J.; Pan, F.; Hu, J.; Wang, M.; Liu, H. In Situ Electromagnetic Induction Heating for CO_2 Temperature Swing Adsorption on Magnetic Fe_3O_4/N-Doped Porous Carbon. *Energy Fuels* **2020**, *34*, 14439−14446.
(40) Huck, J. M.; Lin, L.-C.; Berger, A. H.; Shahrak, M. N.; Martin, R. L.; Bhown, A. S.; Haranczyk, M.; Reuter, K.; Smit, B. Evaluating Different Classes of Porous Materials for Carbon Capture. *Energy Environ. Sci.* **2014**, *7*, 4132−4146.
(41) Lawson, S.; Baamran, K.; Newport, K.; Rezaei, F.; Rownaghi, A. A. Screening of Adsorbent/Catalyst Composite Monoliths for Carbon Capture-Utilization and Ethylene Production. *ACS Appl. Mater. Interfaces* **2021**, *13*, 55198−55207.
(42) Gong, Y.; Chen, C.; Lively, R. P.; Walton, K. S. Humid Ethylene/Ethane Separation on Ethylene-Selective Materials. *Ind. Eng. Chem. Res.* **2021**, *60*, 9940−9947.
(43) Gong, Y.; Cai, X.; You, W.; Jiang, X.; Liu, W.; Lively, R.; Walton, K. S.; Sholl, D. S. Selective Uptake of Ethane/Ethylene Mixtures by UTSA-280 Is Driven by Reversibly Coordinated Water Defects. *Chem. Mater.* **2023**, *35*, 2956−2966.

https://doi.org/10.1021/acssuschemeng.3c01468
ACS Sustainable Chem. Eng. 2023, 11, 8603−8614